Universiteit Leiden
The Netherlands

Hybrid-DFT molecular dynamics simulations of photocatalytic water oxidation in a [Ru-bda]–dye complex

Haas, T. de; Calvani, D.; Zaaruolo, A.; Jong, T. de; Rutgers, J.; Kreupeling, B.; ... ; Buda, F.

Citation
Haas, T. de, Calvani, D., Zaaruolo, A., Jong, T. de, Rutgers, J., Kreupeling, B., ... Buda, F. (2024). Hybrid-DFT molecular dynamics simulations of photocatalytic water oxidation in a [Ru-bda]–dye complex. *The Journal Of Physical Chemistry Part C*, *128*(47), 20093-20103. doi:10.1021/acs.jpcc.4c05104

Version: Publisher's Version
License: Creative Commons CC BY 4.0 license
Downloaded from: https://hdl.handle.net/1887/4175463

Note: To cite this publication please use the final published version (if applicable).

THE JOURNAL OF PHYSICAL CHEMISTRY C
A JOURNAL OF THE AMERICAN CHEMICAL SOCIETY

Open Access
This article is licensed under CC-BY 4.0

pubs.acs.org/JPCC
Article

Hybrid-DFT Molecular Dynamics Simulations of Photocatalytic Water Oxidation in a [Ru-bda]−Dye Complex

Titus de Haas,* Dario Calvani, Aegir Zaaruolo, Tjeerd de Jong, Jonas Rutgers, Bas Kreupeling, Huub J. M. de Groot, and Francesco Buda*

Cite This: J. Phys. Chem. C 2024, 128, 20093−20103
Read Online

ACCESS | Metrics & More | Article Recommendations | Supporting Information

ABSTRACT: In the past decade, Ru-bda (bda = 2,2′-bipyridine-6,6′-dicarboxylic acid) complexes have emerged as extremely effective water oxidation catalysts, rendering them a potential candidate for incorporation into dye-sensitized photoelectrochemical cells. However, the performance of these catalysts declines dramatically when anchored to a photoanode surface due to their catalytic mechanism involving the interaction of two metal centers (I2M). This reduced performance prompts an investigation into the catalytic cycle following an alternative mechanism in which the O−O bond is formed through a water nucleophilic attack (WNA). In this work, we have performed hybrid-DFT based molecular dynamics simulations of the rate-determining O−O bond formation following the WNA mechanism in a [Ru-bda]−dye dyad model in explicit water solvation. In addition, our study probes oxygen dissociation from the Ru^{III}−O_2 intermediate, and the equilibrium dynamics of the low-valent Ru^{III}−bda intermediate. Our simulations demonstrate that including a fraction of exact Hartree−Fock exchange impacts the electron and hole localizations in the catalyst−dye complex, which can in specific instances affect the dynamics of the system. This study contributes to a fundamental understanding of water oxidation catalysis with the Ru-bda catalyst family and highlights the relevance of modeling catalytic processes at the hybrid-DFT level.

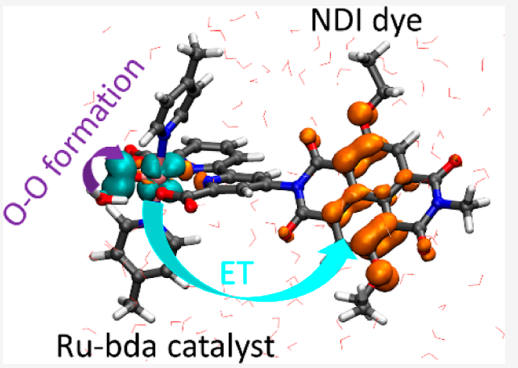

1. INTRODUCTION

In view of an escalating global climate crisis, harnessing solar energy for fuel production stands as a promising endeavor, offering a potential route toward the mitigation of greenhouse gas emissions.[1−4] Dye-sensitized photoelectrochemical cells (DS-PEC) are devices that use sunlight to convert water and other abundant chemical resources into solar fuels.[5,6] Typically, a DS-PEC contains two compartments. At the anode compartment, four photons are used to oxidize two molecules of water into four protons, four electrons, and one molecule of oxygen (O_2). At the cathode of the cell, the acquired reduction potential and the protons are used to generate molecular hydrogen or reduce a carbon-based feedstock into a denser energy carrier such as ethanol or ethylene.[7]

At the anode of the DS-PEC, three chemical components are responsible for the water-splitting process: the semiconductor surface, a water oxidation catalyst (WOC) and a dye molecule. Photon absorption by a dye molecule initiates a charge separation process. The excited dye can donate an electron into the semiconductor surface, usually TiO_2, and donate a hole to the WOC. This last step provides the driving force for one of the proton-coupled electron transfer (PCET) steps that constitute the water oxidation catalytic cycle. In practice, many photoresponsive anodes are based on solid state materials with an activity which is often hampered by slow reaction kinetics and inefficient photoactivity of the semiconductors.[8] In contrast to solid state catalysts, specific molecular catalysts have been reported that perform at much lower overpotentials, in some cases even reaching higher activities than photosystem II.[9,10] In light of this, it becomes highly compelling to adopt a design wherein the catalyst and dye molecules are present in a homogeneous solution or codeposited on the semiconductor surface. However, a major disadvantage of such approaches is that the charge recombination reaction, in which the oxidized dye is quenched by electron−hole recombination from the TiO_2 surface, becomes competitive with the hole-scavenging of the catalyst.[11] To overcome this issue, intermolecularly linked dye−catalyst complexes have been synthesized, either through covalent interactions,[12,13] or through supramolecular assembly strategies.[11] In these photoanodes, the interfacial electron transfer is typically very fast and the efficiency is proposed to be hampered by the chemical conversion rate of the catalyst.[14]

Received: July 29, 2024
Revised: October 27, 2024
Accepted: November 6, 2024
Published: November 14, 2024

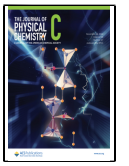

Downloaded via LEIDEN UNIV on November 28, 2024 at 12:08:08 (UTC).
See https://pubs.acs.org/sharingguidelines for options on how to legitimately share published articles.

ACS Publications
© 2024 The Authors. Published by American Chemical Society

https://doi.org/10.1021/acs.jpcc.4c05104
J. Phys. Chem. C 2024, 128, 20093−20103

One class of water oxidation catalysts that has shown to be particularly promising was developed in the laboratories of Sun and Llobet.[9,15] This family of complexes employs a ruthenium center bearing a bda^{2-} (=2,2′-bipyridine-6,6′-dicarboxylic acid) ligand in the equatorial plane and two monodentate pyridyl-type ligands on the axial positions. Because the Ru valence shell in the Ru^{II}−bda complex is completely occupied, the complex becomes catalytically active only after an initial oxidation to form a Ru^{III} species. The tetra-coordinated bda^{2-} backbone leads to a distorted octahedral environment around the ruthenium atom, leaving space for a water molecule to coordinate. However, whether that leads to a 7-coordinated environment around the Ru^{III} center remains a matter of debate, as the flexible bda^{2-} ligand has also been shown to be able to lower its coordination number, either by elongation of one of the equatorial $Ru-N_{bda^{2-}}$ bonds ($k^3-O^2N^1$ binding mode) or by elongation of the $Ru-O_{COO^-}$ distance ($k^3-O^1N^2$ binding mode).[16−18] As the dynamic behavior of this low-valent complex in solution is still not entirely understood, a DFT-based molecular dynamics (DFT-MD) investigation of the coordination chemistry of this complex is desirable.

The Ru-bda family of catalysts typically performs the rate-limiting oxygen−oxygen bond-forming step through a bimolecular mechanism in which two Ru^{V}=O species couple to form a $Ru^{IV}-O-O-Ru^{IV}$ complex that can eventually dissociate O_2.[9,19] This interaction of two metal (I2M) mechanism is postulated to be the major reason for a high catalytic activity of this catalyst class. As a result of its excellent performance, the Ru-bda catalyst has been used as a prototype to study water oxidation in systems where catalysts have been immobilized on surfaces, in supramolecular structures, and even in lipid bilayers and metal−organic frameworks.[20−24] It remains questionable, however, whether the high performance of this catalyst is preserved once the intermolecular collision frequency is significantly reduced as a result of catalyst immobilization. A recent study has shown that after immobilization on TiO_2, the catalyst activity was quenched significantly, even though a second-order kinetics in the catalyst concentration was preserved.[22] This is particularly interesting, since under such conditions a different mechanism is typically expected to become dominant in ruthenium based catalysts.[25] In this alternative mechanism, the O−O bond is formed through a nucleophilic attack of a solvent water molecule on the high valent Ru^{V}=O, culminating in formation of the $Ru^{IV}-O-OH$ intermediate (WNA pathway). After a fourth PCET step, a $Ru^{III}-O_2$ species could be formed, leading to dissociation of the dioxygen ligand to recover the initial catalyst. The amount of work published on the WNA mechanism is significantly less than that on the I2M mechanism in the Ru-bda family, and an in-depth investigation of this alternative catalytic cycle, as well as an estimation of the reaction barriers, is appropriate.

In this work, we performed DFT-MD simulations of all four, proton-coupled electron transfer steps of the WNA mechanism in a Ru-bda catalyst, covalently bound to a naphthalene diimide (NDI) dye in explicit water solvation. Including the electron-accepting NDI and the proton-accepting water environment explicitly, allowed us to study the proton and electron transfer events during the simulation. This work addresses two questions regarding the catalytic cycle of the Ru-bda^{2-} catalyst class. First, we aim to establish a comprehensive picture of the equilibrium dynamics of the low-valent Ru^{III} intermediate, which is still a debated topic in literature. Second, we evaluate the suitability of this catalyst for DS-PEC devices. Specifically, we determine the barrier for O−O bond formation following a nucleophilic attack of a water molecule on the Ru^{V}=O intermediate, and we investigate the O_2 dissociation from the catalyst after the final PCET step.

Over the past three decades, density functional theory (DFT) based on the generalized gradient approximation (GGA) has become the workhorse of DFT-MD due to its numerical efficiency and accurate predictive power when it comes to thermodynamic properties and structures. Despite its extensive use in modeling molecular water oxidation catalysis,[26−31] GGA−DFT is known to suffer from a large self-interaction error, which leads to overdelocalized charge distributions.[32−34] This has been clearly demonstrated for Cl^- ions in water and ineffective hole-localizations in materials and surfaces.[33,35] By applying the Auxiliary Density Matrix Method (ADMM),[36] we could afford to include exact exchange and perform simulations at the hybrid-DFT level, which can correct the overdelocalization errors.[35] Next to addressing the previously posed questions regarding the Ru-bda catalyst, this study also aims to assess the effects of including a fraction of (screened-) Hartree−Fock exchange in the description of the electronic structure.

The applied computational methodologies are described in Section 2. The performed DFT-based molecular dynamics simulations of PCET reactions are discussed in more detail in Section 3. Section 3.1 describes the equilibrium dynamics of the low-valent Ru^{III}−bda intermediate. Section 3.2 deals with the enhanced sampling simulations of the O−O bond formation step, while Section 3.3 investigates the oxygen dissociation from the catalyst after the fourth PCET reaction. The conclusions of this paper are presented in Section 4.

2. COMPUTATIONAL METHODS

The optimized initial structure of the dye-$[Ru(bda)(pic)(OH)]^+$ complex was already obtained in a previous computational work.[37] The complex was placed in a cubic box with periodic boundary conditions. 199 explicit water molecules were added using the PACKMOL[38] builder tool in the AMS2022.102 package by SCM.[39] Subsequently, GROMACS was used to perform classical molecular dynamics (MD) simulations in which the water solvent molecules were equilibrated.[40] In these simulations, the water molecules were modeled with the TIP-3P force field, while the LigParGen tool was used to generate a set of OPLS-AA parameters for the nonmetal atoms in the WOC−dye complex.[41−45] As this tool does not allow for metal parameter optimization, the ruthenium atom was replaced with a seven-coordinated sulfur atom during the optimization run, and the ε and σ van der Waals parameters for ruthenium itself were obtained from Bernardes et al. (see Supporting Information for the employed OPLS-AA force field parameters).[46] Partial charges for all atoms of the WOC−dye complex were obtained from the Mulliken charges calculated at the B3LYP-D3(BJ)/TZP level on the optimized geometry.[37] In these classical MD equilibration runs, the atoms in the WOC−dye complex were kept at fixed positions. After an initial geometry relaxation, 5 ns of *NVT* ensemble simulation followed by 10 ns of *NPT* ensemble simulation were performed, each with a 2 fs time step. These simulations employed the Berendsen thermostat and the Parrinello−Rahman barostat, respectively.[47−49] The volume equilibration yielded a cubic box with a side length of 20.343 Å and the temperature was stable around 300 K (see

https://doi.org/10.1021/acs.jpcc.4c05104
J. Phys. Chem. C 2024, 128, 20093−20103

Supporting Information, Figure S1). This system was subsequently used as the input for the DFT-MD simulations. Before the production runs, additional *NVT* simulations were performed at the DFT-MD level to equilibrate the whole system including the WOC−dye complex at 300 K. These calculations were performed with the Canonical Sampling Through Velocity Rescaling (CSVR) thermostat with a time constant set to 20 fs. The production runs were performed with a time constant of 150 fs. The time evolution of the temperatures of these runs is provided in the Supporting Information, Figure S2.

All Kohn−Sham density functional theory simulations were carried out with the Quickstep routine in the CP2K8.2 software package.[50] All pure-DFT calculations were performed with the PBE exchange−correlation functional, while hybrid-DFT simulations were performed at the B3LYP level. All simulations included Grimme's pairwise additive D3 dispersion corrections with a cutoff of 22 Å and grid-smoothening.[51−54] The valence electrons for ruthenium were modeled with the DZVP-MOLOPT-SR-GTH basis set, while all other elements were modeled with the DZVP-MOLOPT-GTH basis.[55] The core electrons were described using the GTH pseudopotentials optimized for the PBE functional.[56−58] A value of 280 Ry was used as cutoff for the auxiliary plane wave (PW) basis. The PW integration was performed on a 5-layer multigrid with the relative cutoff parameter set to 40 Ry. The orbital transformation (OT) method was used for the SCF procedure, employing a preconditioner based on diagonalization and inversion of the complete $\mathbf{H}-\varepsilon^0\mathbf{S}$ matrix in conjunction with the conjugated gradient minimizer.[59] The convergence accuracy was set to 10^{-6} Hartree, which was found to conserve the total energy in the molecular dynamics simulations. Hybrid-DFT calculations were performed with the B3LYP functional containing a 0.2 fraction of screened Hartree−Fock exchange (HFX).[60−63] The HFX part was computed in an auxiliary density matrix using the AUX_FIT cFIT11 basis for ruthenium and the AUX_FIT cFIT3 basis for all other elements.[36] To reduce the computational cost, the Coulomb operator for the HFX calculation was truncated at a radius of 8.0 a_0 and the threshold for the $\varepsilon_{\text{Schwartz}}$ screening parameter was set to 10^{-6}, with screening of the initial density matrix enabled.[64] Level of theory benchmarks on the structural and electronic properties of the complexes and on the oxygen−oxygen radial distribution function are provided in the Supporting Information Section S7. These tests demonstrate that the level of theory employed is sufficiently accurate for the system of interest in this work.

3. RESULTS AND DISCUSSION

In this work, the $[Ru^{II}(bda)(pic)_2(H_2O)]^+$ (bda = 2,2′-bipyridine-6,6′-dicarboxylic acid, pic = 4-picoline) complex was considered as the water oxidation catalyst. This catalyst has been reported to operate with a catalytic turnover frequency (TOF) of 32 s^{-1} and is representative of a class of ruthenium-based catalysts developed in the groups of Sun and Llobet.[9] Although other catalysts have been reported to perform at higher turnover frequencies, these catalysts typically rely on different axial ligands which increase $\pi-\pi$ stacking interactions, leading to higher intermolecular collision frequencies that favor the I2M pathway.[15,19] Since the purpose of this work is to study the mononuclear WNA mechanism, it is reasonable to consider the smaller 4-picoline ligand, as this saves computational resources. We note that the catalyst with 4-picoline axial ligands has been reported to perform very similarly to its phenylpyridine counterpart once it had been immobilized in a supramolecular assembly on a TiO_2 surface (see ref 11, Figure 2b). This type of catalyst has been adopted in several studies on catalyst and photosensitizer functionalized photoanodes.[11,20,21,65−74]

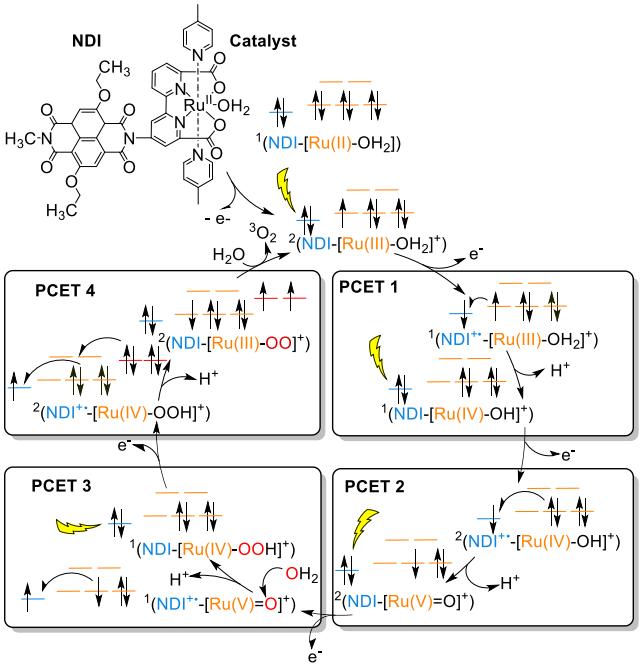

Figure 1. Proposed catalytic cycle for the studied WOC−dye system. Initially, the Ru(II) complex is oxidized to Ru(III). Then, four photoinduced PCET steps lead to formation of one dioxygen molecule, four protons and four electrons. A schematic representation of the electronic configuration on the ruthenium center at each intermediate is depicted in orange and the HOMO energy level of the dye is depicted in blue. The photo-oxidation events are highlighted by the yellow flash symbols. In the third and fourth PCET steps, the high valent ruthenium is reduced with electrons coming from the hydroperoxo/oxygen ligand. Those orbitals are depicted in red. Both in PCET step 1 and step 3, the singlet spin-multiplicity is preserved during the reaction, despite the initial open shell character of the system.

The organic 2,6-diethoxy-1,4,5,8-diimidenapthalene (NDI) dye was employed as photon absorber. This dye has been studied extensively and computational work has shown that it has the appropriate redox properties to provide a driving force for all four PCET steps in the water oxidation process in similar catalysts.[75−77] The NDI molecule was covalently bound to the catalyst on the nitrogen position of one of the imide moieties (see Figure 1). Computational work in our group has shown that photoinduced electron injection from the NDI to the TiO_2 surface is fast compared to the kinetics of the catalyst,[78,79] which is consistent with experimental works on other dye-TiO_2 interfaces.[80−82] The TiO_2 was, therefore, not taken into account explicitly and the photoinduced electron injection was simulated by instantaneous oxidation of the dye molecule. Experimental works, as well as in silico efforts, have focused on elucidating the reaction mechanism for the $[Ru^{II}(bda)(pic)_2(H_2O)]^+$ catalyst.[15] Based on these investigations and the research reported in this work, a reaction mechanism is proposed for the catalyst-dye complex. The

https://doi.org/10.1021/acs.jpcc.4c05104
J. Phys. Chem. C 2024, 128, 20093−20103

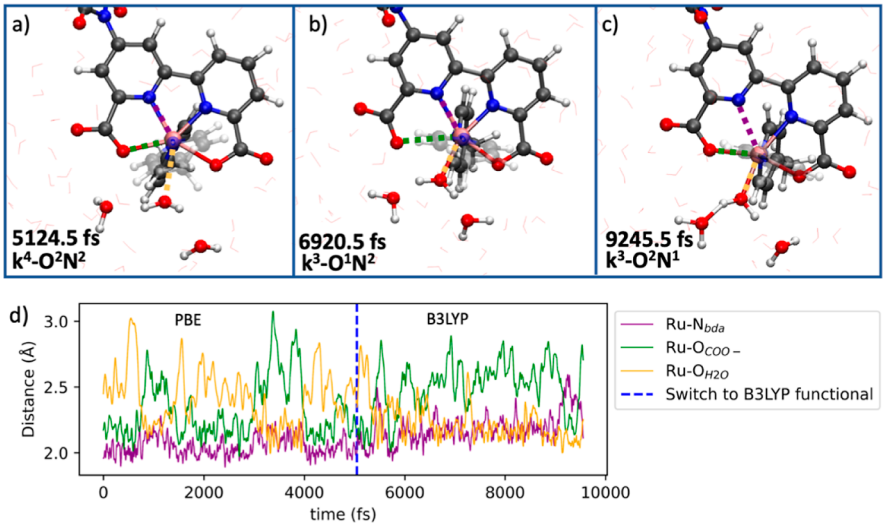

Figure 2. Snapshots from the AIMD simulations that represent the three binding modes, $k^4-O^2N^2$ (a), $k^3-O^1N^2$ (b) and $k^3-O^2N^1$ (c), are displayed in the top panel. The time evolution of Ru−$N_{bda^{2-}}$, Ru−O_{COO^-} and Ru−O_{H_2O} bonds are plotted in (d). In panel (d), the first half of the trajectory is propagated at the GGA−PBE level, while the second half of the trajectory is propagated at the hybrid-B3LYP level of theory.

proposed catalytic cycle is depicted in Figure 1. The catalyst is activated by oxidation of the Ru^{II} complex to form a $Ru^{III}-OH_2$ intermediate. Subsequently, a series of four proton coupled electron transfer steps lead to formation of $Ru^{IV}-OH$, $Ru^{V}=O$, $Ru^{IV}-OOH$ and finally again the $Ru^{III}-OH_2$. It has been found in earlier research that during the entire catalytic cycle the ruthenium remains in the low-spin electronic configuration.[83] In this work, we have simulated with DFT based molecular dynamics all four PCET steps of the catalyst-dye complex. Simulations of the first and second PCET step were found to proceed on a fast time scale and are discussed in the Supporting Information Sections S3 and S4. The first section in the results concerns the equilibrium dynamics of the Ru^{III}-bda intermediate before the first PCET step, as the nature of this equilibrium is still under debate in literature. Subsequently, the paper focuses on the rate-limiting third PCET step and the fourth PCET step which is rapidly followed by release of the dioxygen ligand.

3.1. Probing the Equilibrium Dynamics of the Low-Valent Ru^{III}-bda Intermediate. From a combination of X-ray, NMR, and EPR studies, three distinct binding modes have been resolved for Ru^{III}−bda complexes.[16−18] In the first binding mode, one of the carboxylate groups is reported to dissociate from the ruthenium, leading to a $k^3-O^1N^2$ coordination, whereas in the second binding mode the Ru−$N_{bda^{2-}}$ is elongated, leading to a $k^3-O^2N^1$ coordination.[17,18] More recently, also a complex has been isolated in which the aqua ligand exhibits a weak interaction with the ruthenium, while the bda^{2-} backbone binds symmetrically in a $k^4-O^2N^2$ binding mode.[16] In order to gain insights into the dynamic behavior of the catalyst in this low-valent oxidation state, we performed simulations both employing the PBE and the B3LYP exchange−correlation functionals. The ^{2}(NDI-[Ru-(III)−OH^2])$^+$ complex was equilibrated at the GGA−PBE level for 3 ps and subsequently propagated for another 5 ps at room temperature. Then the simulation was continued for another 4.6 ps at the hybrid level.

Interestingly, the complex was found to exhibit a dynamic equilibrium in which all binding modes discussed above participate. Snapshots of the trajectory where the system is in the $k^4-O^2N^2$, $k^3-O^1N^2$ and $k^3-O^2N^1$ binding modes are provided in Figure 2a, b and c, respectively. These figures also indicate with colors the Ru−O_{H_2O}, Ru−O_{COO^-} and Ru−$N_{bda^{2-}}$ bonds that coordinate and dissociate from the ruthenium center. The time evolution of these bonds during the PBE and B3LYP simulations is visualized in Figure 2d. The other Ru−O_{COO^-} and Ru−$N_{bda^{2-}}$ distances, as well as the axial Ru-N_{pic} distances, were found to remain relatively stable during the MD simulation and are provided in the Supporting Information, Figures S3 and S4. In the performed PBE-based simulations, it was found that the system resides in a dynamic equilibrium between two six-coordinated, pseudo-octahedral complexes, where the aqua ligand and one of the bda-carboxyl group rapidly coordinate and dissociate to the Ru^{III} center on the sub-ps time scale. Interestingly, the binding of the aqua ligand was paired with the formation of strong hydrogen bonding interactions between the aqua ligand and the surrounding water molecules. Remarkably, at the B3LYP level of theory the dynamic behavior of the complex was preserved, but now also involving the $k^3-O^2N^1$ binding mode, where the equatorial Ru−$N_{bda^{2-}}$ distance is elongated, see parts of the trajectory between 5.2 and 5.4 ps and 9.1−9.5 ps in Figure 2. It was also attempted to equilibrate this $k^3-O^2N^1$ complex at the PBE level by constraining the equatorial Ru−$N_{bda^{2-}}$ distance to 2.54 Å and equilibrating the system for 2.5 ps. However, after lifting the constraint the system was found to relax instantaneously to the $k^3-O^1N^2$ coordination mode.

It can be concluded that the barriers associated with the transitions between the different binding modes are low. The aqua ligand is found to remain in close proximity of the metal center (<3.0 Å) at all times during the simulation, even in the case of $k^4-O^2N^2$ coordination of the bda^{2-} ligand. This pseudo 7-coordinated environment implies that the first step in the catalytic cycle is not limited by slow coordination of the aqua ligand to the Ru(III) center. These results underscore how DFT-MD with explicit solvent can help to understand the dynamical flexibility in the coordination sphere of transition metal complexes.

3.2. Blue Moon Simulations of the Rate-Determining O−O Bond Formation Step. The first and second

https://doi.org/10.1021/acs.jpcc.4c05104
J. Phys. Chem. C 2024, 128, 20093−20103

photoinduced proton-coupled electron transfer (PCET) steps in the catalytic cycle of the investigated catalyst-dye dyad were found to proceed fast, on the ab initio MD time scale of several picoseconds (see Supporting Information, Sections S3 and S4). Consequently, we shift our attention to the third PCET event (PCET 3 in Figure 1). We employed a similar strategy as in the previous section: the equilibration of the system and exploratory Metadynamics (MetaD) and Blue Moon ensemble simulations were performed at the GGA−PBE level of theory, followed by an additional ∼1 ps propagation of the Blue Moon ensemble trajectories at the hybrid-B3LYP level to refine the results. This approach enables us to compare the obtained free energy surface (FES) at both levels of theory. This section describes in more detail the performed enhanced sampling simulations.

The high-valent ^{2}(NDI-[Ru(V)═O])$^+$ complex was equilibrated at room temperature for ∼4 ps at the GGA−PBE level of theory. During this simulation, the spin density was localized exclusively on the ruthenium t2g and the oxygen p orbitals (see Supporting Information, Section S5, Figure S8). Despite the considerable electron deficient character of the oxygen, essentially no nucleophilic coordination of water molecules was observed in the performed simulations. This is in accordance with other in silico studies that reported the Ru═O moiety to be hydrophobic.[19] The Ru−O distance was found to fluctuate around 1.72 ± 0.05 Å, which is in excellent agreement with in situ X-ray absorption spectroscopy studies on this catalyst class, that report a value of 1.75 ± 0.02 Å.[84] At this stage, the complex was found strictly in the 7-coordinated environment with a symmetric binding of the carboxyl groups, although both Ru−O bonds fluctuated appreciably. After the removal of one alpha-spin electron from the dye, the system was found to equilibrate to a stable open-shell singlet with one unpaired alpha-electron on the catalyst and one unpaired beta-electron on the dye (see Figure S9). This complex was found to remain stable over the course of 3 ps, without attempting electron transfer or interaction with nearby water molecules.

In order to observe the slow O−O bond formation, the water nucleophilic attack was accelerated by employing the well-tempered MetaD enhanced sampling method, of which the details are discussed in Supporting Information Section S6.1.[85] The O−O distance between the oxo ligand and the nearest water molecule in the solvent was chosen as collective variable (CV), similarly to previous studies.[26,29,75] We argue that this choice of the CV is justified, given that one cannot discriminate between different water molecules in the simulation and the system is sufficiently equilibrated before we start the MetaD. Notably, the carboxylate group of the bda^{2-} ligand acted as a hydrogen bond acceptor toward one of the protons of the nucleophilic water molecule during the final ∼22 ps of the MetaD simulation, even though this interaction was not included in the collective variable along which the reaction was biased (see Figure 3). Nevertheless, the PCET event consistently involved dissociation of the proton facing the water environment, and not the one involved in this interaction. Although the MetaD simulations yielded a reactive trajectory, the statistical error in the obtained free energy surface (FES) remained large within the time scale that we could afford to run the simulation (see Supporting Information, Figure S10).

The FES was further refined following the Blue Moon approach using the O−O distance as collective variable.[86,87] Nine structures were sampled from the MetaD simulation with

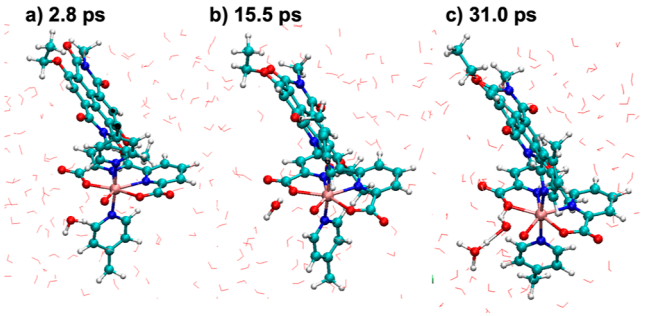

Figure 3. Three stages during the third PCET reaction, forming the O−O bond. (a) The water molecule roams around freely. (b) One of the protons on the water molecule forms a hydrogen bond with the carboxylate group of the bda^{2-} ligand. (c) The O−O bond is formed, while simultaneously the water facing proton is abstracted following a Grotthüs mechanism.

O−O distances between 3.0 and 1.4 Å at 0.2 Å intervals. These structures were subsequently used as input for GGA−PBE based MD simulations, in which their O−O distance was constrained. After the averaged constraint force λ for each MD simulation had converged to a stable value, the trajectories were propagated for another $1.5 < t < 3$ ps, after which a constraint force profile was constructed from the averaged λ values (see Supporting Information, Figure S11a). Two additional points were added to this profile at 1.45 and 3.3 Å, which were found to be the equilibrium O−O distances in the reactant and product states of the reaction from unconstrained reactions (see Supporting Information, Section S6.2). The profile was fitted with a 100-point Akima spline, and subsequently numerically integrated to obtain the FES (see Supporting Information, Figure S11b). The already equilibrated GGA−PBE trajectories were further propagated for another ∼1 ps at the hybrid-B3LYP level, after which this procedure was repeated to generate the force profile and FES at the hybrid-DFT level (Figure 4a,b). To improve the resolution in the region of the transition state, two additional points, at 2.1 and 1.9 Å, were considered at the hybrid-level. Errors on the λ-profile and FES were obtained from block averaging. Details on this procedure and further details on the Blue Moon approach are provided in the Supporting Information, Section S6.2.

The hybrid-B3LYP based Blue Moon ensemble simulations predict a 20.3 ± 1.2 kcal mol^{-1} free energy barrier governing the O−O bond formation. The overall reaction has a free energy difference of 1.8 ± 1.9 kcal mol^{-1}, indicating that within the statistical error there is no significant thermodynamic driving force with the selected NDI dye. Previous studies from our group on different catalysts with the same dye showed a larger driving force for the O−O bond formation, likely because those catalysts involved Ru in a lower oxidation state.[75,76] Experimentally, the half wave potential $E_{1/2}$ for the employed NDI dye has been measured at 1.36 V vs Fc/Fc$^+$,[88] which thus appears to be the minimum required oxidation potential for mononuclear water oxidation catalysis with this Ru-bda catalyst.[77] While the relatively low barrier suggests the viability of the WNA mechanism as a potential route, the associated rate constant of ∼0.008 s^{-1} (min = 0.001 s^{-1}, max = 0.06 s^{-1}) is 4 to 8 orders of magnitude slower than the rates achieved through the I2M mechanism with this catalyst.[15] We have also calculated the reaction profile at the GGA−PBE level (see the Supporting Information, Figure S11). Interestingly,

https://doi.org/10.1021/acs.jpcc.4c05104
J. Phys. Chem. C 2024, 128, 20093−20103

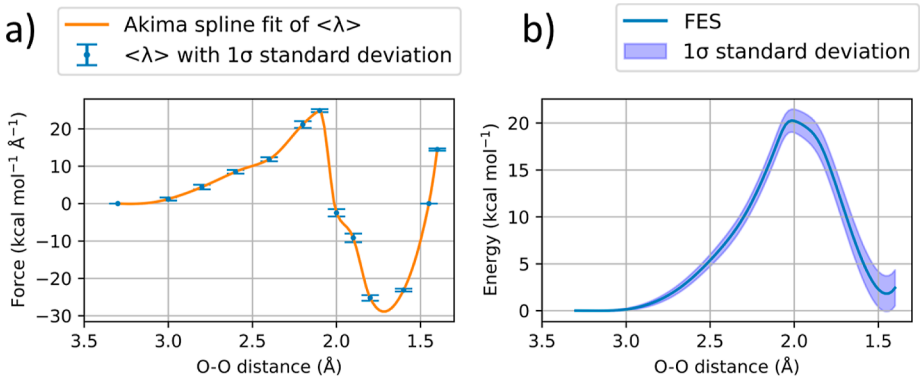

Figure 4. FES calculated at the B3LYP level, plotted as a function of the O−O distance reaction coordinate. The free energy was obtained by thermodynamic integration of a 100-point Akima spline fit of the averaged constraint forces, $\langle\lambda\rangle$, at different values of the constrained O−O bond distance. The error bars on $\langle\lambda\rangle$ are obtained by block averaging. The error on the FES is calculated by integrating the upper and lower bounds of the $\langle\lambda\rangle$ profile.

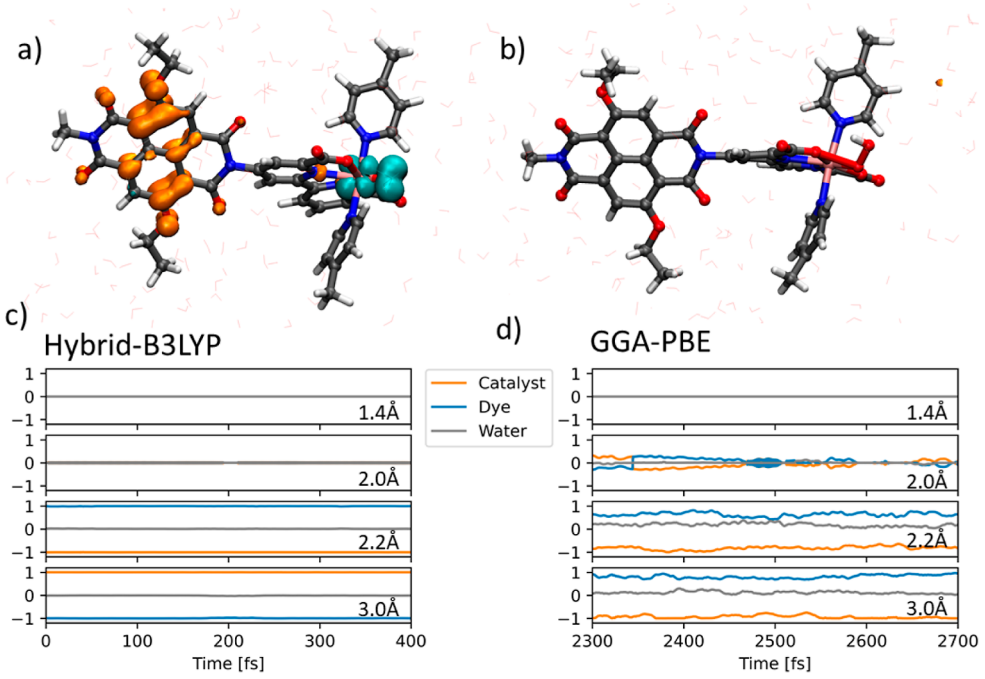

Figure 5. Top panels provide a visualization of the spin density of snapshots taken from the hybrid-B3LYP simulations with constrained O−O distances of 3.0 Å (a) and 1.4 Å (b), where the isosurface values were set to 0.003 for positive, and −0.003 for negative spin density contributions. Panels (c,d) plot the spin density population analysis on the catalyst (orange), dye (blue) and water (gray) as a function of simulation time. The local spin density on the specified fragments was obtained by summing over the atomic Mulliken spin density contributions.

the overall reaction is found to be endothermic at that level with a ΔG = 2.9 ± 0.9 kcal mol^{-1}. The barrier at the GGA-level is lower than at the hybrid-level, with the $\Delta G^{\ddagger}$ = 14.9 ± 0.9 kcal mol^{-1}. Note that the error bar at the GGA-level is smaller than at the hybrid-B3LYP level since GGA is computationally more efficient and simulations can be run over a longer time scale.

To get a better understanding of the observed differences between the two functional set-ups, we have evaluated the proton and electron transfer dynamics during the Blue Moon ensemble simulations. In these simulations, the proton involved in the PCET reaction was not constrained and, therefore, free to dissociate from the nucleophilic water molecule. Similarly, the electron could move freely from the catalyst to the photo-oxidized dye. In Figure 5, panel a, the spin density of the initial state corresponding to an open-shell singlet spin configuration with an unpaired electron on the catalyst and a hole on the dye is shown (see also Figure 1, PCET 3). After the third PCET step, a singlet closed shell configuration is obtained, where the unpaired electron on the catalyst has recombined with the hole (Figure 5, panel b). In Figure 5, panels c and d, the hybrid-B3LYP and GGA−PBE spin density evolution is visualized for the duration of 400 fs during the Blue Moon simulations with constrained O−O distances of 3.0, 2.2, 2.0 and 1.4 Å. Figure 5c displays the first 400 fs for the hybrid simulations, while Figure 5d provides the 400 fs in which the PCET event takes places in the 2.0 Å GGA-based simulation.

Figure 5 shows that the simulations with constrained O−O distances longer than 2.0 Å exhibit consistently an open shell singlet spin-multiplicity, where the hole is located on the dye. The application of the pure-DFT functional leads to a

https://doi.org/10.1021/acs.jpcc.4c05104
J. Phys. Chem. C 2024, 128, 20093−20103

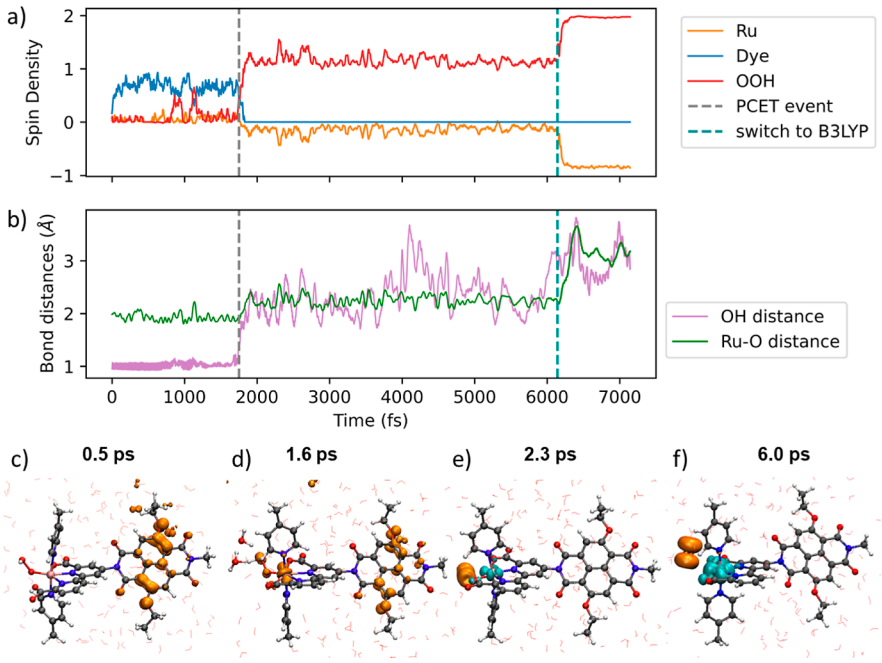

Figure 6. (a) The red, blue, and orange traces represent the integrated spin moments on the O−O ligand, NDI dye, and ruthenium center, respectively. (b) The purple line represents the length of the dissociating O−H bond, while the green line represents the Ru−O distance. (c−f) provide visualizations of the spin density at four stages which are characteristic for the PCET reaction. Isosurface values were set to 0.003 for positive, and −0.003 for negative spin density contributions.

considerable fraction of spin density on the water solvent molecules. This is a commonly known artifact of GGA-based DFT.[33,34] Interestingly, this spin delocalization is virtually eliminated in the simulations with the hybrid-B3LYP functional. The tendency of B3LYP to localize the spin density better than PBE becomes particularly apparent when the O−O distance is shortened to 2.2 Å. At that point, the integrated spin density on the dye is reduced to ∼0.6 at the GGA level, indicating that the electron and hole are formed only partially. In contrast, the spin localization on the dye is still preserved entirely at the hybrid-B3LYP level. The GGA simulation at 2.0 Å shows that the electron−hole pair separation collapses after 2500 fs, which was found to coincide with the proton transfer event. In the simulations with an O−O bond distance shorter than 2.0 Å, the system forms consistently a closed-shell singlet, where the electron has transferred to the dye.

3.3. Dioxygen Dissociation after the Fourth PCET Step. The initial structure for the equilibration simulations of the $^{1}([Ru(IV)\text{-}OOH]\text{-}NDI)^{+}$ intermediate was extracted from the final part of the trajectory of the third PCET step, where the excess proton was removed from the water solvation environment. The system was equilibrated at the PBE level at room temperature for 2 ps before once more the photooxidation of the NDI was simulated by removing an electron from the simulation box. The evolution of the spin density on the dye, catalyst, and the water environment are plotted over time in Figure 6a in the top panel, while the dissociating O−H distance from the hydroperoxo ligand is shown in Figure 6b.

Although the hole is initially delocalized on the solvent water molecules, the majority of the spin density localizes on the NDI within the first ∼100 fs after oxidation of the system (Figure 6a,c). In the following ∼1.7 ps the system remains in a stable state where the proton is still attached to the O−O ligand. Interestingly, two attempted electron transfers are observed prior to the final PCET event, at around 0.9 and 1.1 ps. At this stage, a water molecule is closely coordinated to the hydroperoxo ligand, however, there is no chain of water molecules to facilitate long-range proton transfer. Subsequently, a second water molecule was observed to form a hydrogen bond interaction with the water molecule coordinating to the hydroperoxo ligand, allowing for the PCET event to occur (see Figure 6d). After the PCET, significant oscillations are observed of the spin density moving between the metal center and the oxygen ligand. Nevertheless, the performed simulations employing the PBE functional eventually appeared to favor a configuration where one of the triplet oxygen electrons recombines with the antiferromagnetically coupled ruthenium electron, forming what is best described as a doublet spin configuration on the oxygen ligand (see Figure 6e). This species remained stable over more than 4 ps of simulation time. Since GGA functionals are known to overestimate charge delocalization, it was decided to propagate the system for another 1 ps with the B3LYP functional.[32−34] By including a fraction of (screened-) Hartree−Fock exchange, the previously observed spin-delocalization was now eliminated, and two unpaired electrons localized on the dioxygen ligand exclusively, forming a local triplet (see Figure 6f). Consequently, the O_2 ligand dissociated rapidly from the catalyst after switching to the hybrid functional. This observation underlines the importance of including a fraction of exact exchange in this type of simulations and should be kept in mind for future studies on similar systems.

4. CONCLUSIONS

In summary, DFT-based molecular dynamics simulations were performed of the four proton-coupled electron transfer (PCET) steps in the catalytic water oxidation cycle of a $[Ru^{III}(bda)(pic)_2(H_2O)]^{+}$ (bda = 2,2′-bipyridine-6,6′-dicarboxylic acid, pic = 4-picoline) catalyst, covalently bound to the 2,6-diethoxy-1,4,5,8-diimidenapthalene (NDI) dye. The first

https://doi.org/10.1021/acs.jpcc.4c05104
J. Phys. Chem. C 2024, 128, 20093−20103

part of this work addresses the coordination environment of the ruthenium center at the beginning of the catalytic cycle. The dynamics simulations reveal that the low-valent $[Ru^{III}(bda)(pic)_2(H_2O)]^+$ intermediate adopts a six-coordinated configuration, wherein coordination of the aqua ligand is followed by a lowering of the coordination number of the bda^{2-} ligand, either by elongation of the equatorial $Ru-N_{bda^{2-}}$ bond or by elongation of the equatorial $Ru-O_{COO^-}$ bond. Following the first PCET step, the resulting $[Ru^{IV}(bda)(pic)_2(OH)]^+$ complex consistently maintained a 7-coordinated environment. This 7-coordinated environment is preserved also after the second, third, and fourth PCET steps.

To gain an understanding of the behavior of this catalyst when anchored to a surface, the O−O bond-forming step was considered to involve the nucleophilic attack of a water molecule on a single, high-valent $Ru^V{=}O$ species. Using Blue Moon ensemble simulations at the B3LYP level, the barrier for this process was determined to be 20.3 ± 1.2 kcal mol^{-1}, corresponding to a catalytic rate of approximately 0.008 s^{-1} (min = 0.001 s^{-1}, max = 0.06 s^{-1}) at 300 K. This rate represents a realistic estimate for systems where the catalyst is immobilized, and is 4 to 8 orders of magnitude slower than the rates that have been reported in studies where the catalyst followed the binuclear mechanism.[9,15] The oxidation potential of the employed NDI dye, which has been measured at 1.36 V vs Fc/Fc^+,[88] was found to be slightly insufficient to drive the O−O bond formation. We found that the subsequent and final PCET step, in which the hydroperoxo ligand is oxidized to form O_2, happened spontaneously on the ab initio molecular dynamics time scale and will, therefore, not affect much the kinetics of the catalyst.

Finally, we have evaluated the performance of the widely used GGA−PBE and the hybrid-B3LYP functionals in determining the reaction barriers, energetics, and description of spin localizations in the DFT-based molecular dynamics simulations. In addition to the slight changes in the relative energies of reactant and product states for the rate-determining O−O bond formation, it was found that the GGA functional exhibits a tendency to overestimate delocalization of spin density, leading to significant spin polarizations on the water environment and unphysical pairing of electrons on the O_2 ligand with an electron on the ruthenium center. Interestingly, the inclusion of exact exchange virtually removed the excess delocalization, leading to the electron and hole densities being localized exclusively on the catalyst and dye fragments of the system. The most notable effect of this correction on the dynamics was observed for the dissociation of the O_2 ligand at the end of the catalytic cycle, which happened spontaneously with the hybrid functional while in the simulations with the GGA functional the oxygen molecule remained bound to the ruthenium complex.

■ ASSOCIATED CONTENT

Data Availability Statement

The data that support the findings of this study are available from the corresponding author upon reasonable request.

Supporting Information

The Supporting Information is available free of charge at https://pubs.acs.org/doi/10.1021/acs.jpcc.4c05104.

Section S1 deals with the calculation of rate constants. Section S2 displays the equilibration of the different investigated intermediates. Sections S3 and 4 cover the first and second PCET steps in the proposed catalytic cycle. Section S5 shows the spin densities of catalytic intermediates in the doublet spin state, and Section S6 provides extensive details on the applied enhanced sampling methods and calculation of the error bars. Section S7 provides benchmarks for the level of theory used (PDF)

■ AUTHOR INFORMATION

Corresponding Authors

Titus de Haas − *Leiden Institute of Chemistry, Leiden University, 2333CC Leiden, The Netherlands;* orcid.org/0000-0002-2206-3219; Email: t.de.haas@lic.leidenuniv.nl

Francesco Buda − *Leiden Institute of Chemistry, Leiden University, 2333CC Leiden, The Netherlands;* orcid.org/0000-0002-7157-7654; Email: f.buda@chem.leidenuniv.nl

Authors

Dario Calvani − *Leiden Institute of Chemistry, Leiden University, 2333CC Leiden, The Netherlands;* orcid.org/0000-0002-3106-4061

Aegir Zaaruolo − *Leiden Institute of Chemistry, Leiden University, 2333CC Leiden, The Netherlands;* orcid.org/0009-0007-1672-2947

Tjeerd de Jong − *Leiden Institute of Chemistry, Leiden University, 2333CC Leiden, The Netherlands*

Jonas Rutgers − *Leiden Institute of Chemistry, Leiden University, 2333CC Leiden, The Netherlands*

Bas Kreupeling − *Leiden Institute of Chemistry, Leiden University, 2333CC Leiden, The Netherlands;* orcid.org/0000-0002-5954-0218

Huub J. M. de Groot − *Leiden Institute of Chemistry, Leiden University, 2333CC Leiden, The Netherlands;* orcid.org/0000-0002-8796-1212

Complete contact information is available at: https://pubs.acs.org/10.1021/acs.jpcc.4c05104

Notes

The authors declare no competing financial interest.

■ ACKNOWLEDGMENTS

This work was sponsored by NWO−Domain Science for the use of supercomputer facilities.

■ REFERENCES

(1) Ardo, S.; Fernandez Rivas, D.; Modestino, M. A.; Schulze Greiving, V.; Abdi, F. F.; Alarcon Llado, E.; Artero, V.; Ayers, K.; Battaglia, C.; Becker, J. P.; et al. Pathways to Electrochemical Solar-Hydrogen Technologies. *Energy Environ. Sci.* **2018**, *11*, 2768−2783.

(2) Tian, H. Solid-State p-Type Dye-Sensitized Solar Cells: Progress, Potential Applications and Challenges. *Sustainable Energy Fuels* **2019**, *3*, 888−898.

(3) Kim, J. H.; Hansora, D.; Sharma, P.; Jang, J.-W.; Lee, J. S. Toward Practical Solar Hydrogen Production − an Artificial Photosynthetic Leaf-to-Farm Challenge. *Chem. Soc. Rev.* **2019**, *48*, 1908−1971.

(4) Haussener, S. Solar Fuel Processing: Comparative Mini-Review on Research, Technology Development, and Scaling. *Sol. Energy* **2022**, *246*, 294−300.

(5) Grätzel, M. Photoelectrochemical cells. *Nature* **2001**, *414*, 338−344.

(6) Vilanova, A.; Dias, P.; Lopes, T.; Mendes, A. The Route for Commercial Photoelectrochemical Water Splitting: A Review of

Large-Area Devices and Key Upscaling Challenges. *Chem. Soc. Rev.* **2024**, *53*, 2388−2434.
(7) Nitopi, S.; Bertheussen, E.; Scott, S. B.; Liu, X.; Engstfeld, A. K.; Horch, S.; Seger, B.; Stephens, I. E. L.; Chan, K.; Hahn, C.; et al. Progress and Perspectives of Electrochemical CO 2 Reduction on Copper in Aqueous Electrolyte. *Chem. Rev.* **2019**, *119*, 7610−7672.
(8) Seo, J.; Nishiyama, H.; Yamada, T.; Domen, K. Visible-Light-Responsive Photoanodes for Highly Active, Stable Water Oxidation. *Angew. Chem., Int. Ed.* **2018**, *57*, 8396−8415.
(9) Duan, L.; Bozoglian, F.; Mandal, S.; Stewart, B.; Privalov, T.; Llobet, A.; Sun, L. A Molecular Ruthenium Catalyst with Water-Oxidation Activity Comparable to That of Photosystem II. *Nat. Chem.* **2012**, *4*, 418−423.
(10) Yang, J.; Wang, L.; Zhan, S.; Zou, H.; Chen, H.; Ahlquist, M. S. G.; Duan, L.; Sun, L. From Ru-Bda to Ru-Bds: A Step Forward to Highly Efficient Molecular Water Oxidation Electrocatalysts under Acidic and Neutral Conditions. *Nat. Commun.* **2021**, *12*, 373.
(11) Li, H.; Li, F.; Wang, Y.; Bai, L.; Yu, F.; Sun, L. Visible-Light-Driven Water Oxidation on a Photoanode by Supramolecular Assembly of Photosensitizer and Catalyst. *ChemPlusChem* **2016**, *81*, 1056−1059.
(12) Ashford, D. L.; Song, W.; Concepcion, J. J.; Glasson, C. R. K.; Brennaman, M. K.; Norris, M. R.; Fang, Z.; Templeton, J. L.; Meyer, T. J. Photoinduced Electron Transfer in a Chromophore−Catalyst Assembly Anchored to TiO 2. *J. Am. Chem. Soc.* **2012**, *134*, 19189−19198.
(13) Alibabaei, L.; Brennaman, M. K.; Norris, M. R.; Kalanyan, B.; Song, W.; Losego, M. D.; Concepcion, J. J.; Binstead, R. A.; Parsons, G. N.; Meyer, T. J. Solar Water Splitting in a Molecular Photoelectrochemical Cell. *Proc. Natl. Acad. Sci. U.S.A.* **2013**, *110*, 20008−20013.
(14) Kirner, J. T.; Stracke, J. J.; Gregg, B. A.; Finke, R. G. Visible-Light-Assisted Photoelectrochemical Water Oxidation by Thin Films of a Phosphonate-Functionalized Perylene Diimide Plus CoO_x Cocatalyst. *ACS Appl. Mater. Interfaces* **2014**, *6*, 13367−13377.
(15) Zhang, B.; Sun, L. Ru-Bda: Unique Molecular Water-Oxidation Catalysts with Distortion Induced Open Site and Negatively Charged Ligands. *J. Am. Chem. Soc.* **2019**, *141*, 5565−5580.
(16) Liu, T.; Li, G.; Shen, N.; Wang, L.; Timmer, B. J. J.; Zhou, S.; Zhang, B.; Kravchenko, A.; Xu, B.; Ahlquist, M. S. G.; et al. Isolation and Identification of Pseudo Seven-Coordinate Ru(III) Intermediate Completing the Catalytic Cycle of Ru-Bda Type of Water Oxidation Catalysts. *CCS Chem.* **2022**, *4*, 2481−2490.
(17) Matheu, R.; Ghaderian, A.; Francàs, L.; Chernev, P.; Ertem, M. Z.; Benet-Buchholz, J.; Batista, V. S.; Haumann, M.; Gimbert-Suriñach, C.; Sala, X.; et al. Behavior of Ru-Bda Water-Oxidation Catalysts in Low Oxidation States. *Chem.—Eur. J.* **2018**, *24*, 12838−12847.
(18) Daniel, Q.; Huang, P.; Fan, T.; Wang, Y.; Duan, L.; Wang, L.; Li, F.; Rinkevicius, Z.; Mamedov, F.; Ahlquist, M. S. G.; et al. Rearranging from 6- to 7-Coordination Initiates the Catalytic Activity: An EPR Study on a Ru-Bda Water Oxidation Catalyst. *Coord. Chem. Rev.* **2017**, *346*, 206−215.
(19) Zhan, S.; Mårtensson, D.; Purg, M.; Kamerlin, S. C. L.; Ahlquist, M. S. G. Capturing the Role of Explicit Solvent in the Dimerization of Ru V (Bda) Water Oxidation Catalysts. *Angew. Chem., Int. Ed.* **2017**, *56*, 6962−6965.
(20) Wang, D.; Marquard, S. L.; Troian-Gautier, L.; Sheridan, M. V.; Sherman, B. D.; Wang, Y.; Eberhart, M. S.; Farnum, B. H.; Dares, C. J.; Meyer, T. J. Interfacial Deposition of Ru(II) Bipyridine-Dicarboxylate Complexes by Ligand Substitution for Applications in Water Oxidation Catalysis. *J. Am. Chem. Soc.* **2018**, *140*, 719−726.
(21) Wang, D.; Eberhart, M. S.; Sheridan, M. V.; Hu, K.; Sherman, B. D.; Nayak, A.; Wang, Y.; Marquard, S. L.; Dares, C. J.; Meyer, T. J. Stabilized Photoanodes for Water Oxidation by Integration of Organic Dyes, Water Oxidation Catalysts, and Electron-Transfer Mediators. *Proc. Natl. Acad. Sci. U.S.A.* **2018**, *115*, 8523−8528.
(22) Yan, X.; Sakai, K.; Ozawa, H. Highly Efficient and Stable Molecular-Based TiO 2 Photoanodes for Photoelectrochemical Water Splitting Achieved by Pyridyl Anchoring Technique. *ACS Catal.* **2023**, *13*, 13456−13465.
(23) Song, H.; Amati, A.; Pannwitz, A.; Bonnet, S.; Hammarström, L. Mechanistic Insights into the Charge Transfer Dynamics of Photocatalytic Water Oxidation at the Lipid Bilayer−Water Interface. *J. Am. Chem. Soc.* **2022**, *144*, 19353−19364.
(24) Feng, J.; Li, X.; Luo, Y.; Su, Z.; Zhong, M.; Yu, B.; Shi, J. Microenvironment Regulation of Ru(Bda)L2 Catalyst Incorporated in Metal-Organic Framework for Effective Photo-Driven Water Oxidation. *Chin. J. Catal.* **2023**, *48*, 127−136.
(25) Shaffer, D. W.; Xie, Y.; Concepcion, J. J. O−O Bond Formation in Ruthenium-Catalyzed Water Oxidation: Single-Site Nucleophilic Attack vs. O−O Radical Coupling. *Chem. Soc. Rev.* **2017**, *46*, 6170−6193.
(26) Govindarajan, N.; Tiwari, A.; Ensing, B.; Meijer, E. J. Impact of the Ligand Flexibility and Solvent on the O−O Bond Formation Step in a Highly Active Ruthenium Water Oxidation Catalyst. *Inorg. Chem.* **2018**, *57*, 13063−13066.
(27) Schilling, M.; Cunha, R. A.; Luber, S. Zooming in on the O−O Bond Formation - An Ab Initio Molecular Dynamics Study Applying Enhanced Sampling Techniques. *J. Chem. Theory Comput.* **2020**, *16*, 2436−2449.
(28) Schilling, M.; Ketkaew, R.; Luber, S. How Ab Initio Molecular Dynamics Can Change the Understanding on Transition Metal Catalysed Water Oxidation. *Chimia* **2021**, *75*, 195−201.
(29) Schilling, M.; Cunha, R. A.; Luber, S. Enhanced Ab Initio Molecular Dynamics Exploration Unveils the Complex Role of Different Intramolecular Bases on the Water Nucleophilic Attack Mechanism. *ACS Catal.* **2020**, *10*, 7657−7667.
(30) Gorantla, K. R.; Mallik, B. S. Iron Complex as a Water-Oxidizing Catalyst: Free-Energy Barriers, Proton-Coupled Electron Transfer, Spin Dynamics, and Role of Water Molecules in the Reaction Mechanism. *J. Phys. Chem. C* **2020**, *124*, 205−218.
(31) Gorantla, K. R.; Mallik, B. S. Mechanistic Insights into Cobalt-Based Water Oxidation Catalysis by DFT-Based Molecular Dynamics Simulations. *J. Phys. Chem. A* **2022**, *126*, 3301−3310.
(32) Cohen, A. J.; Mori-Sánchez, P.; Yang, W. Insights into Current Limitations of Density Functional Theory. *Science* **2008**, *321*, 792−794.
(33) Li, C.; Zheng, X.; Su, N. Q.; Yang, W. Localized Orbital Scaling Correction for Systematic Elimination of Delocalization Error in Density Functional Approximations. *Natl. Sci. Rev.* **2018**, *5*, 203−215.
(34) Bryenton, K. R.; Adeleke, A. A.; Dale, S. G.; Johnson, E. R. Delocalization Error: The Greatest Outstanding Challenge in Density-functional Theory. *Wiley Interdiscip. Rev.: Comput. Mol. Sci.* **2023**, *13*, No. e1631.
(35) Cheng, J.; Sulpizi, M.; VandeVondele, J.; Sprik, M. Hole Localization and Thermochemistry of Oxidative Dehydrogenation of Aqueous Rutile TiO 2 (110). *ChemCatChem* **2012**, *4*, 636−640.
(36) Guidon, M.; Hutter, J.; VandeVondele, J. Auxiliary Density Matrix Methods for Hartree−Fock Exchange Calculations. *J. Chem. Theory Comput.* **2010**, *6*, 2348−2364.
(37) de Haas, T.; van Overeem, H.; de Groot, H. J. M.; Buda, F. Strategies to Enhance the Rate of Proton-Coupled Electron Transfer Reactions in Dye-Water Oxidation Catalyst Complexes. *ChemPhotoChem* **2023**, *7*, No. e202200274.
(38) Martínez, L.; Andrade, R.; Birgin, E. G.; Martínez, J. M. PACKMOL: A Package for Building Initial Configurations for Molecular Dynamics Simulations. *J. Comput. Chem.* **2009**, *30*, 2157−2164.
(39) Rüger, R.; Franchini, M.; Trnka, T.; Yakovlev, A.; van Lenthe, E.; Philipsen, P.; van Vuren, T.; Klumpers, B.; Soini, T. AMS2021.*101*, SCM, Theoretical Chemistry, Vrije Universiteit Amsterdam, Amsterdam, 2021. http://www.scm.com.
(40) Van Der Spoel, D.; Lindahl, E.; Hess, B.; Groenhof, G.; Mark, A. E.; Berendsen, H. J. C. GROMACS: Fast, Flexible, and Free. *J. Comput. Chem.* **2005**, *26*, 1701−1718.

https://doi.org/10.1021/acs.jpcc.4c05104
J. Phys. Chem. C 2024, 128, 20093−20103

(41) Jorgensen, W. L.; Chandrasekhar, J.; Madura, J. D.; Impey, R. W.; Klein, M. L. Comparison of Simple Potential Functions for Simulating Liquid Water. *J. Chem. Phys.* **1983**, *79*, 926−935.
(42) Jorgensen, W. L.; Maxwell, D. S.; Tirado-Rives, J. Development and Testing of the OPLS All-Atom Force Field on Conformational Energetics and Properties of Organic Liquids. *J. Am. Chem. Soc.* **1996**, *118*, 11225−11236.
(43) Dodda, L. S.; Cabeza de Vaca, I.; Tirado-Rives, J.; Jorgensen, W. L. LigParGen Web Server: An Automatic OPLS-AA Parameter Generator for Organic Ligands. *Nucleic Acids Res.* **2017**, *45*, W331−W336.
(44) Jorgensen, W. L.; Tirado-Rives, J. Potential Energy Functions for Atomic-Level Simulations of Water and Organic and Biomolecular Systems. *Proc. Natl. Acad. Sci. U.S.A.* **2005**, *102*, 6665−6670.
(45) Dodda, L. S.; Vilseck, J. Z.; Tirado-Rives, J.; Jorgensen, W. L. 1.14*CM1A-LBCC: Localized Bond-Charge Corrected CM1A Charges for Condensed-Phase Simulations. *J. Phys. Chem. B* **2017**, *121*, 3864−3870.
(46) Bernardes, C. E. S.; Canongia, L.; José, N.; Da Piedade, M. E. M. All-Atom Force Field for Molecular Dynamics Simulations on Organotransition Metal Solids and Liquids. Application to M(CO)n (M = Cr, Fe, Ni, Mo, Ru, or W) Compounds. *J. Phys. Chem. A* **2013**, *117*, 11107−11113.
(47) Berendsen, H. J. C.; Postma, J. P. M.; Van Gunsteren, W. F.; DiNola, A.; Haak, J. R. Molecular Dynamics with Coupling to an External Bath. *J. Chem. Phys.* **1984**, *81*, 3684−3690.
(48) Parrinello, M.; Rahman, A. Polymorphic Transitions in Single Crystals: A New Molecular Dynamics Method. *J. Appl. Phys.* **1981**, *52*, 7182−7190.
(49) Nosé, S.; Klein, M. L. Constant Pressure Molecular Dynamics for Molecular Systems. *Mol. Phys.* **1983**, *50*, 1055−1076.
(50) Kühne, T. D.; Iannuzzi, M.; Del Ben, M.; Rybkin, V. V.; Seewald, P.; Stein, F.; Laino, T.; Khaliullin, R. Z.; Schütt, O.; Schiffmann, F.; et al. CP2K: An Electronic Structure and Molecular Dynamics Software Package - Quickstep: Efficient and Accurate Electronic Structure Calculations. *J. Chem. Phys.* **2020**, *152*, 194103.
(51) Perdew, J. P.; Burke, K.; Ernzerhof, M. Generalized Gradient Approximation Made Simple [Phys. Rev. Lett. 77, 3865 (1996)]. *Phys. Rev. Lett.* **1997**, *78*, 1396.
(52) Grimme, S. Accurate Description of van Der Waals Complexes by Density Functional Theory Including Empirical Corrections. *J. Comput. Chem.* **2004**, *25*, 1463−1473.
(53) Grimme, S. Density Functional Theory with London Dispersion Corrections. *Wiley Interdiscip. Rev.: Comput. Mol. Sci.* **2011**, *1*, 211−228.
(54) Grimme, S. Supramolecular Binding Thermodynamics by Dispersion-Corrected Density Functional Theory. *Chem.—Eur. J.* **2012**, *18*, 9955−9964.
(55) VandeVondele, J.; Hutter, J. Gaussian Basis Sets for Accurate Calculations on Molecular Systems in Gas and Condensed Phases. *J. Chem. Phys.* **2007**, *127*, 114105.
(56) Goedecker, S.; Teter, M.; Hutter, J. Separable Dual-Space Gaussian Pseudopotentials. *Phys. Rev. B: Condens. Matter Mater. Phys.* **1996**, *54*, 1703−1710.
(57) Hartwigsen, C.; Goedecker, S.; Hutter, J. Relativistic Separable Dual-Space Gaussian Pseudopotentials from H to Rn. *Phys. Rev. B: Condens. Matter Mater. Phys.* **1998**, *58*, 3641−3662.
(58) Krack, M. Pseudopotentials for H to Kr Optimized for Gradient-Corrected Exchange-Correlation Functionals. *Theor. Chem. Acc.* **2005**, *114*, 145−152.
(59) VandeVondele, J.; Hutter, J. An Efficient Orbital Transformation Method for Electronic Structure Calculations. *J. Chem. Phys.* **2003**, *118*, 4365−4369.
(60) Becke, A. D. Density-Functional Exchange-Energy Approximation with Correct Asymptotic Behavior. *Phys. Rev. A* **1988**, *38*, 3098−3100.
(61) Becke, A. D. A New Mixing of Hartree-Fock and Local Density-Functional Theories. *J. Chem. Phys.* **1993**, *98*, 1372−1377.
(62) Vosko, S. H.; Wilk, L.; Nusair, M. Accurate Spin-Dependent Electron Liquid Correlation Energies for Local Spin Density Calculations: A Critical Analysis. *Can. J. Phys.* **1980**, *58*, 1200−1211.
(63) Stephens, P. J.; Devlin, F. J.; Chabalowski, C. F.; Frisch, M. J. Ab Initio Calculation of Vibrational Absorption and Circular Dichroism Spectra Using Density Functional Force Fields. *J. Phys. Chem.* **1994**, *98*, 11623−11627.
(64) Guidon, M.; Schiffmann, F.; Hutter, J.; VandeVondele, J. Ab Initio Molecular Dynamics Using Hybrid Density Functionals. *J. Chem. Phys.* **2008**, *128*, 214104.
(65) Li, L.; Duan, L.; Xu, Y.; Gorlov, M.; Hagfeldt, A.; Sun, L. A Photoelectrochemical Device for Visible Light Driven Water Splitting by a Molecular Ruthenium Catalyst Assembled on Dye-Sensitized Nanostructured TiO2. *Chem. Commun.* **2010**, *46*, 7307.
(66) Gao, Y.; Ding, X.; Liu, J.; Wang, L.; Lu, Z.; Li, L.; Sun, L. Visible Light Driven Water Splitting in a Molecular Device with Unprecedentedly High Photocurrent Density. *J. Am. Chem. Soc.* **2013**, *135*, 4219−4222.
(67) Li, H.; Li, F.; Zhang, B.; Zhou, X.; Yu, F.; Sun, L. Visible Light-Driven Water Oxidation Promoted by Host−Guest Interaction between Photosensitizer and Catalyst with A High Quantum Efficiency. *J. Am. Chem. Soc.* **2015**, *137*, 4332−4335.
(68) Li, F.; Fan, K.; Wang, L.; Daniel, Q.; Duan, L.; Sun, L. Immobilizing Ru(Bda) Catalyst on a Photoanode via Electrochemical Polymerization for Light-Driven Water Splitting. *ACS Catal.* **2015**, *5*, 3786−3790.
(69) Gao, Y.; Zhang, L.; Ding, X.; Sun, L. Artificial Photosynthesis − Functional Devices for Light Driven Water Splitting with Photoactive Anodes Based on Molecular Catalysts. *Phys. Chem. Chem. Phys.* **2014**, *16*, 12008.
(70) Sherman, B. D.; Xie, Y.; Sheridan, M. V.; Wang, D.; Shaffer, D. W.; Meyer, T. J.; Concepcion, J. J. Light-Driven Water Splitting by a Covalently Linked Ruthenium-Based Chromophore−Catalyst Assembly. *ACS Energy Lett.* **2017**, *2*, 124−128.
(71) Eberhart, M. S.; Wang, D.; Sampaio, R. N.; Marquard, S. L.; Shan, B.; Brennaman, M. K.; Meyer, G. J.; Dares, C.; Meyer, T. J. Water Photo-Oxidation Initiated by Surface-Bound Organic Chromophores. *J. Am. Chem. Soc.* **2017**, *139*, 16248−16255.
(72) Zhang, L.; Gao, Y.; Ding, X.; Yu, Z.; Sun, L. High-Performance Photoelectrochemical Cells Based on a Binuclear Ruthenium Catalyst for Visible-Light-Driven Water Oxidation. *ChemSusChem* **2014**, *7*, 2801−2804.
(73) Wang, D.; Sheridan, M. V.; Shan, B.; Farnum, B. H.; Marquard, S. L.; Sherman, B. D.; Eberhart, M. S.; Nayak, A.; Dares, C. J.; Das, A. K.; et al. Layer-by-Layer Molecular Assemblies for Dye-Sensitized Photoelectrosynthesis Cells Prepared by Atomic Layer Deposition. *J. Am. Chem. Soc.* **2017**, *139*, 14518−14525.
(74) Yamamoto, M.; Nishizawa, Y.; Chábera, P.; Li, F.; Pascher, T.; Sundström, V.; Sun, L.; Imahori, H. Visible Light-Driven Water Oxidation with a Subporphyrin Sensitizer and a Water Oxidation Catalyst. *Chem. Commun.* **2016**, *52*, 13702−13705.
(75) Shao, Y.; De Ruiter, J. M.; De Groot, H. J. M.; Buda, F. Photocatalytic Water Splitting Cycle in a Dye-Catalyst Supramolecular Complex: Ab Initio Molecular Dynamics Simulations. *J. Phys. Chem. C* **2019**, *123*, 21403−21414.
(76) Shao, Y.; Groot, H. J. M. D.; Buda, F. Tuning the Proton-Coupled Electron-Transfer Rate by Ligand Modification in Catalyst − Dye Supramolecular Complexes for Photocatalytic Water Splitting. *ChemSusChem* **2021**, *14*, 479.
(77) Belić, J.; Förster, A.; Menzel, J. P.; Buda, F.; Visscher, L. Automated Assessment of Redox Potentials for Dyes in Dye-Sensitized Photoelectrochemical Cells. *Phys. Chem. Chem. Phys.* **2021**, *24*, 197−210.
(78) Menzel, J. P.; Papadopoulos, A.; Belić, J.; de Groot, H. J. M.; Visscher, L.; Buda, F. Photoinduced Electron Injection in a Fully Solvated Dye-Sensitized Photoanode: A Dynamical Semiempirical Study. *J. Phys. Chem. C* **2020**, *124*, 27965−27976.
(79) Monti, A.; Negre, C. F. A.; Batista, V. S.; Rego, L. G. C.; De Groot, H. J. M.; Buda, F. Crucial Role of Nuclear Dynamics for

https://doi.org/10.1021/acs.jpcc.4c05104
J. Phys. Chem. C 2024, 128, 20093−20103

Electron Injection in a Dye-Semiconductor Complex. *J. Phys. Chem. Lett.* **2015**, *6*, 2393−2398.
(80) Hilgendorff, M.; Sundström, V. Dynamics of Electron Injection and Recombination of Dye-Sensitized TiO 2 Particles. *J. Phys. Chem. B* **1998**, *102*, 10505−10514.
(81) Ellingson, R. J.; Asbury, J. B.; Ferrere, S.; Ghosh, H. N.; Sprague, J. R.; Lian, T.; Nozik, A. J. Dynamics of Electron Injection in Nanocrystalline Titanium Dioxide Films Sensitized with [Ru(4,4'-Dicarboxy-2,2'-Bipyridine) 2 (NCS) 2] by Infrared Transient Absorption. *J. Phys. Chem. B* **1998**, *102*, 6455−6458.
(82) Asbury, J. B.; Anderson, N. A.; Hao, E.; Ai, X.; Lian, T. Parameters Affecting Electron Injection Dynamics from Ruthenium Dyes to Titanium Dioxide Nanocrystalline Thin Film. *J. Phys. Chem. B* **2003**, *107*, 7376−7386.
(83) Menzel, J. P.; Kloppenburg, M.; Belić, J.; de Groot, H. J. M.; Visscher, L.; Buda, F. Efficient Workflow for the Investigation of the Catalytic Cycle of Water Oxidation Catalysts: Combining GFN-xTB and Density Functional Theory. *J. Comput. Chem.* **2021**, *42*, 1885−1894.
(84) Lebedev, D.; Pineda-Galvan, Y.; Tokimaru, Y.; Fedorov, A.; Kaeffer, N.; Copéret, C.; Pushkar, Y. The Key Ru V = O Intermediate of Site-Isolated Mononuclear Water Oxidation Catalyst Detected by in Situ X-Ray Absorption Spectroscopy. *J. Am. Chem. Soc.* **2018**, *140*, 451−458.
(85) Barducci, A.; Bussi, G.; Parrinello, M. Well-Tempered Metadynamics: A Smoothly Converging and Tunable Free-Energy Method. *Phys. Rev. Lett.* **2008**, *100*, 020603.
(86) Sprik, M.; Ciccotti, G. Free Energy from Constrained Molecular Dynamics. *J. Chem. Phys.* **1998**, *109*, 7737−7744.
(87) Ciccotti, G.; Ferrario, M. Blue Moon Approach to Rare Events. *Mol. Simul.* **2004**, *30*, 787−793.
(88) Kishore, R. S. K.; Kel, O.; Banerji, N.; Emery, D.; Bollot, G.; Mareda, J.; Gomez-Casado, A.; Jonkheijm, P.; Huskens, J.; Maroni, P.; et al. Ordered and Oriented Supramolecular n/p-Heterojunction Surface Architectures: Completion of the Primary Color Collection. *J. Am. Chem. Soc.* **2009**, *131*, 11106−11116.

https://doi.org/10.1021/acs.jpcc.4c05104
J. Phys. Chem. C 2024, 128, 20093−20103